Re-absorption free scintillating hetero-ligand MOFs crystals activated by ultrafast energy transfer

M. Orfano, J. Perego, C.X. Bezuidenhout, Benoit Sabot, Sylvie Pierre, S. Piva, A. Comotti, A. Monguzzi

ADVANCED FUNCTIONAL MATERIALS
www.afm-journal.de

Reabsorption-Free Scintillating Hetero-Ligand MOF Crystals Activated by Ultrafast Energy Transfer

Matteo Orfano, Jacopo Perego, Charl X. Bezuidenhout, Irene Villa, Roberto Lorenzi, Benoit Sabot, Sylvie Pierre, Silvia Bracco, Sergio Piva, Angiolina Comotti, and Angelo Monguzzi**

Fast photoluminescence and scintillation with a Stokes shift larger than 1 eV is achieved in hetero-ligand metal–organic framework (MOF) crystals comprising inorganic linking nodes and fluorescent conjugated ligands. By finely engineering the MOF composition with the use of ligands with strictly complementary emission and absorption properties and highly delocalized molecular electronic orbitals, the singlet excitons diffusion is enhanced through the ligand framework, fully exploiting both Förster and Dexter energy transfer mechanisms. This allows for the sensitization of energy acceptor ligand fluorescence by ultrafast non-radiative energy transfer with a rate up to the THz range. This efficient antenna effect instantly activates the MOF scintillation with a Stokes shift as large as 1.3 eV in the blue spectral range, matching the highest sensitivity spectral window of the best photodetector available. This is obtained using a minimal doping level of the energy acceptor species, with a consequent elimination of emission re-absorption that allows the achievement of a 500% increment of the MOFs scintillation efficiency and the detection of the radioactive krypton isotope ^{85}Kr from the gas phase with an improved sensitivity compared with the reference material.

1. Introduction

Limiting the self-absorption of the luminescence emission to maximize the light output is crucial in many photonic applications, for example in fluorescence bio-imaging to limit stray light, avoiding the use of expensive hardware or post-processing,[1] or in solar applications to prevent reabsorption in luminescent solar concentrators,[2] and especially in the case of luminescent scintillators employed to monitor the ionizing radiations.[1,3] Unfortunately, large Stokes shift materials that exhibit a significant energy difference between absorption and emission energies, such as phosphorescent conjugated chromophores or electronically-doped semiconductor nanocrystals,[3b,4] often show slow emission rates. This hinders their use where large Stokes shift fast emitters are needed for the acquisition of high-quality images in short time frames, such as ToF-PET imaging,[5] for the detection of high-rate/high-energy events to avoid detrimental pile-up of the recorded emitted photons, or to realize sensitive detectors for rare events, such as in the activity quantification of gas radionuclides.[6]

To overcome this problem, we recently demonstrated that both fast scintillation and large Stokes shift emission can be achieved in metal-organic framework (MOF) crystals comprising inorganic linking nodes containing heavy elements prone to interact with the ionizing radiations and highly fluorescent conjugated ligands.[7] By framing ligands with complementary emission and absorption properties for non-radiative energy transfer, we realized a hetero-ligand MOF with a Stokes shift as large as 0.75 eV in the blue to the green region of the visible electromagnetic spectrum.

Here, we push this approach to the limit by further fine-tuning MOF composition and architecture to improve its photophysical and scintillation properties. In order to realize a reabsorption-free fast scintillator that matches the spectral quantum efficiency range of the best photodiodes employed in scintillator detectors, typically peaked in the UV-blue region, we designed and realized a hetero-ligand MOF by co-assembling 2',5'-dimethyl-[1,1':4',1''-terphenyl]-4,4''-dicarboxylate (TP), a UV scintillating dye, and the blue-emitting ligand 4,4'-(anthracene-9,10-diyl)dibenzoate (DPA), linked by Zr oxy-hydroxy nodes (**Figure 1**). The TP and DPA emission and absorption are largely resonant, thus enabling a Förster-type non-radiative energy transfer. Notably, the TP molecular orbitals are delocalized over the entire length of

M. Orfano, J. Perego, C. X. Bezuidenhout, I. Villa, R. Lorenzi, S. Bracco, S. Piva, A. Comotti, A. Monguzzi
Dipartimento di Scienza dei Materiali
Università degli Studi Milano-Bicocca
via R. Cozzi 55, Milano 20125, Italy
E-mail: angiolina.comotti@unimib.it; angelo.monguzzi@unimib.it

B. Sabot, S. Pierre
Laboratoire National Henri Becquerel (LNE-LNHB)
CEA
LIST
Université Paris-Saclay
Palaiseau 91192, France

The ORCID identification number(s) for the author(s) of this article can be found under https://doi.org/10.1002/adfm.202404480

DOI: 10.1002/adfm.202404480

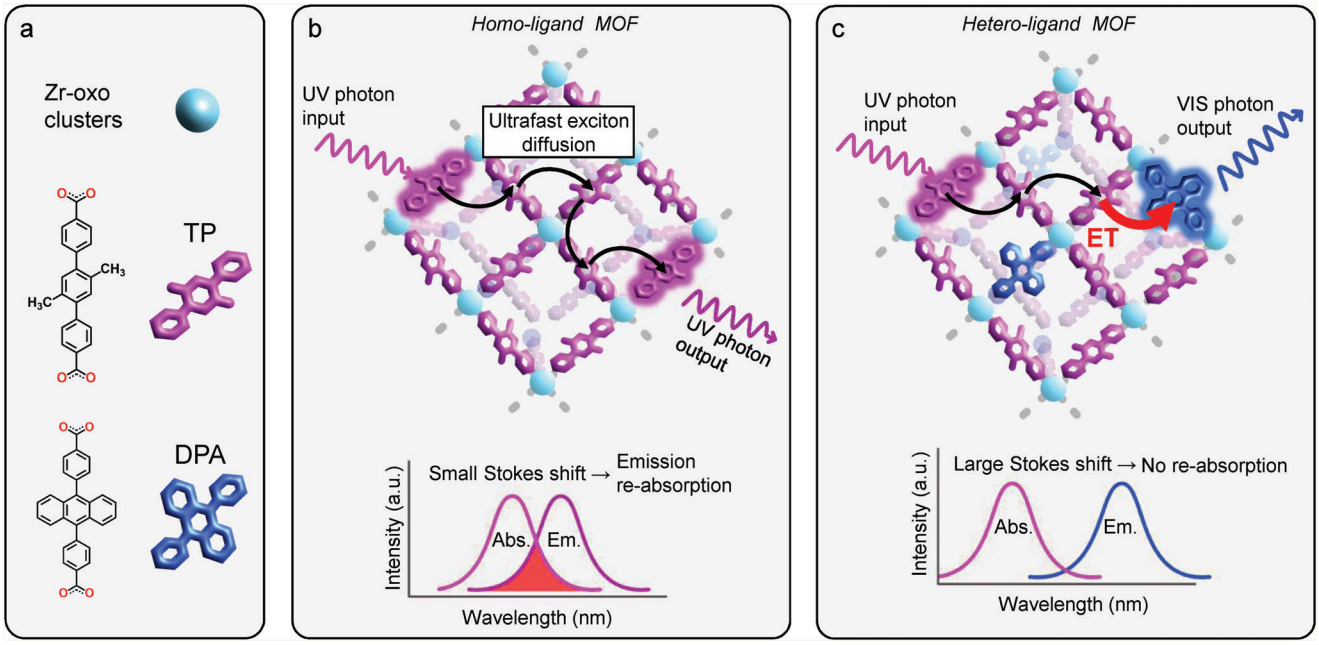

Figure 1. a) Molecular structure of the MOF building blocks, namely the 2',5'-dimethyl-[1,1':4',1''-terphenyl]-4,4''-dicarboxylate (TP) ligand, the 4,4'-(anthracene-9,10-diyl)dibenzoate fluorescent ligand (DPA) and the zirconium node. b,c) Energy flux in the MOF structure after generation of a TP singlet exciton upon absorption of a UV photon. In the homo-ligand MOF, the singlet exciton diffuses within the crystalline framework until radiative recombination. In the hetero-ligand MOF, the singlet exciton diffuses until it reaches the co-ligand DPA. The latter is excited by non-radiative energy transfer and then recombines radiatively by emitting a blue photon with enhanced Stokes shift and, therefore, zero re-absorption of its luminescence.

the ligand main axis. This favors the singlet excitons diffusion through both homo-molecular Förster and Dexter non-radiative energy transfer between neighboring TP ligands, allowing for the sensitization of DPA emissive singlet states through an ultrafast non-radiative energy transfer with a rate that reaches the THz range. This extremely efficient mechanism enables the realization of fast scintillating MOF crystals with an instantaneous activation of their~3 ns lifetime emission at 450 nm. The Stokes shift achieved is larger than 1.3 eV, from the UV to the VIS spectral regions. Notably, this was realized using a minimal doping level of the energy acceptor species, about one order of magnitude lower than the amount of the energy acceptor described in the literature in the best-performing large Stokes shift luminescent MOFs.[7] This efficient antenna mechanism, and the consequent elimination of the emission re-absorption, enabled a five times increase in its scintillation efficiency. In the optimal composition, the hetero-ligand MOF has been tested to capture and detect the radioactive krypton isotope ^{85}Kr from the gas phase, demonstrating a high affinity for this radionuclide and a clearly improved detection sensitivity compared with the reference material.

2. Design and Structural Properties of Hetero-Ligand MOFs

Figure 2 shows the absorption and photoluminescence properties of the two ligands performed on diluted solutions in cyclohexane (10^{-5} M). The TP ligand, i.e. the energy donor in our antenna system, absorbs light in the UV range with a maximum at 300 nm and shows near-UV photoluminescence peaked at 370 nm with a characteristic emission lifetime τ_{TP} = 1.0 ns and photoluminescence quantum yield ϕ_{PL}^{TP}= 0.50±0.05 (Figure 2a; Figure S1, Supporting Information). The DPA moiety shows an absorption peaked at 370 nm, thus perfectly matching the donor emission. Its photoluminescence peaked in the blue spectral region at 420 nm. The emission lifetime is 6.6 ns, with a yield ϕ_{PL}^{DPA}= 0.96±0.10. Their electronic properties have been investigated further by quantum mechanical modeling based on the Time-Dependent Density Functional Theory (TD-DFT).[8,9] Figure 2c,d shows the results obtained for the TP and DPA ligands, respectively. In both cases, the energies of the highest occupied molecular orbital (HOMO) and lowest unoccupied molecular orbital (LUMO) in the ground states mirror the absorption properties of the first HOMO-LUMO electronic transition for TP and DPA (Figures S5–S8 and section S2, Supporting Information). The double-headed arrows in Figure 2c,d mark the orientation of the electric dipole associated with the $S_0 \rightarrow S_1$ electronic transition, which can be used to model both the Förster hopping-mediated diffusion of TP singlets within the crystal framework and the Förster energy transfer to the acceptor DPA ligands (sections S1.1 – S1.3, Supporting Information, Figures S2 and S3; Tables S1 and S2, Supporting Information). Moreover, an in-depth analysis of the shape of the frontier HOMO/LUMO molecular orbitals of the two conjugated ligands highlights another essential property of the system. The DPA frontier molecular orbitals are mainly localized on the central anthracene unit. In contrast, the TP frontier orbitals are delocalized along the main axis of the ligand, thus almost overlapping with the linking nodes. Specifically, the TP ligands in the MOF structure sit at a center-to-center molecular distance of ≈ 1.2 nm (vide

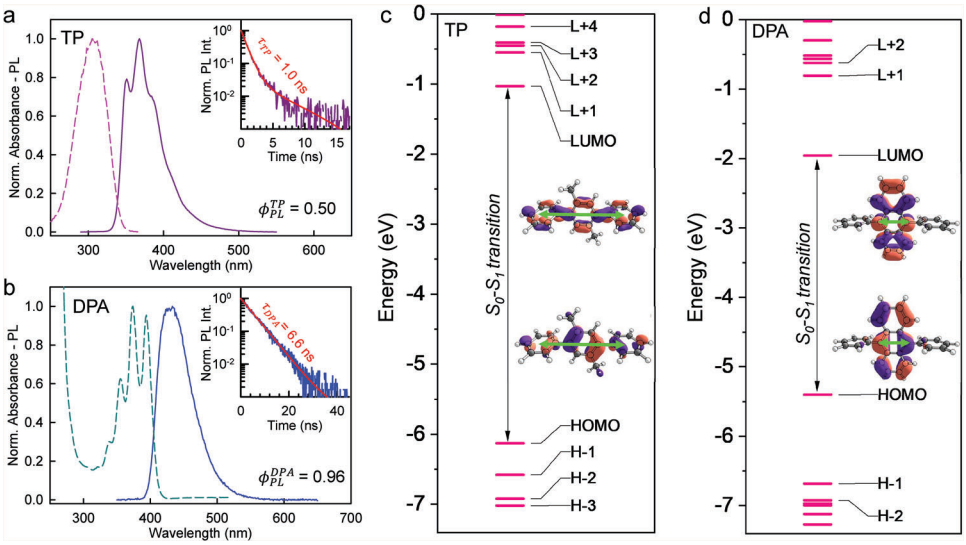

Figure 2. Absorption (dashed line) and photoluminescence (PL, solid line) spectra of TP a) and DPA b) ligands dissolved in cyclohexane (10^{-5} M). The PL spectra are recorded under excitation in the absorption maximum. The inset shows the PL intensity decay as a function of time monitored at the PL emission maximum under pulsed laser excitation (250 nm for TP and 340 nm for DPA, respectively). Solid lines are fit with multi- or single exponential decay functions for TP and DPA, respectively. c,d) Frontier molecular orbitals (HOMO and LUMO) for the organic core of the TP c) and DPA d) ligands. The double-headed arrows show the orientation of the transition electric dipole moments of the $S_0 \rightarrow S_1$ (ground state singlet S_0 and first excited singlet S_1) transition for the two systems. The molecular orbital energy diagrams show the occupied (HOMO, H-x) and unoccupied (LUMO, L-x) frontier orbitals.

infra) that enables dipole-dipole interactions, while the effective spatial separation of the molecular orbital wavefunctions near the linking nodes is reduced to ≈ 0.7 nm, thus activating the exchange interaction between the electrons of adjacent TP units by allowing by the physical overlap of their electronic molecular orbitals wavefunctions.[10,11] This is crucial in determining the effective diffusivity of TP molecular excitons within the framework by enabling the diffusion of singlet TP excitons through both homo-molecular Förster and Dexter energy transfer mechanisms within the TPs ensemble. Therefore, we expect a faster and more efficient diffusion-mediated energy transfer to the DPA co-ligands than previously observed in MOFs made of ligands with strongly localized molecular orbitals.[7]

Zr-based hetero-ligand MOFs[12] were prepared by co-assembly of the DPA and TP ligands in the presence of $ZrOCl_2 \cdot 8H_2O$ under solvothermal conditions modulated by benzoic acid, then followed by activation at 100 °C under vacuum (sections S3 and S4, Supporting Information).[13] The two ligands, which exhibited the same end-to-end length and connectivity, coordinate to Zr-oxy-hydroxy clusters, creating a series of isostructural hetero-ligand MOFs with controlled compositions containing 0.05% to 22.9% DPA molar fraction (denoted Zr-DPA:TP-x%, **Figure 3**). The corresponding homo-ligand MOFs (Zr-DPA and Zr-TP) were prepared for comparison (Table S3, Supporting Information). The composition of the hetero-ligand MOFs were estimated by ^{1}H NMR of digested samples, which are congruent with the feeding ratio (Figure 3a, Figure S10, Table S4, (Figures S49–S55; Tables S10–S12, Supporting Information). The synthesis conditions were optimized to obtain highly reproducible batches of ≈ 200 mg (Figures S56 and S57, Supporting Information). FT-IR spectroscopy of Zr-DPA:TP-x% displayed a reduction of the characteristic band of the carboxylic acid signal at 1686 cm^{-1}, associated with the stretching vibration of C=O, and the appearance of two strong bands centred at 1597 and 1412 cm^{-1}, assigned to the asymmetric and symmetric OCO carboxylate stretching vibrations, respectively, due to the coordination of the carboxylate groups to the Zr-based clusters (Figures S11–S15, Supporting Information). Thermogravimetric analysis showed a high thermal stability for the Zr-DPA:TP-x% MOFs of up to 450 °C. The weight loss between 150 and 325 °C is associated with the de-hydroxylation reaction of the zirconium-based oxo-hydroxy cluster as described in the literature for UiO-66 type MOF (Figures S31–S39, Supporting Information).[14]

The Zr-MOFs displayed high crystallinity and a cubic crystal structure (space group *Fm*-3*m*) with a **fcu** topology (Figure 3b), as established by indexing the PXRD patterns (Figures S25–S30; Tables S5–S8, Supporting Information). The crystal structures of parent Zr-TP and the Zr-DPA:TP-22.9% were resolved by Rietveld refinement of synchrotron-source PXRD patterns collected at 293 K combined with PW-DFT optimizations (Figure S25; Table S5, Supporting Information). Each Zr-based node is coordinated to twelve ligands ($Zr_6(\mu_3\text{-}O)_4(\mu_3\text{-}OH)_4(CO_2)_{12}$ cluster) and generates a framework containing interconnected tetrahedral and octahedral cavities with average volumes equivalent to fitted sphere diameters of 11.5 and 17.2 Å, respectively (Figure 3b). Thus, neighboring ligands are arranged at short intermolecular distances of 11.6 Å (center-to-center of the ligands) and 7.3 Å (center-to-center of the terminal *p*-phenylene rings). The total available pore volume is ≈73% of the crystal structure, as explored by a probe radius of 1.82 Å (kinetic diameter of N_2). The diffraction patterns of the whole series of Zr-MOFs with variable DPA ligand content proved the generation of a family of isoreticular structures with comparable unit cell

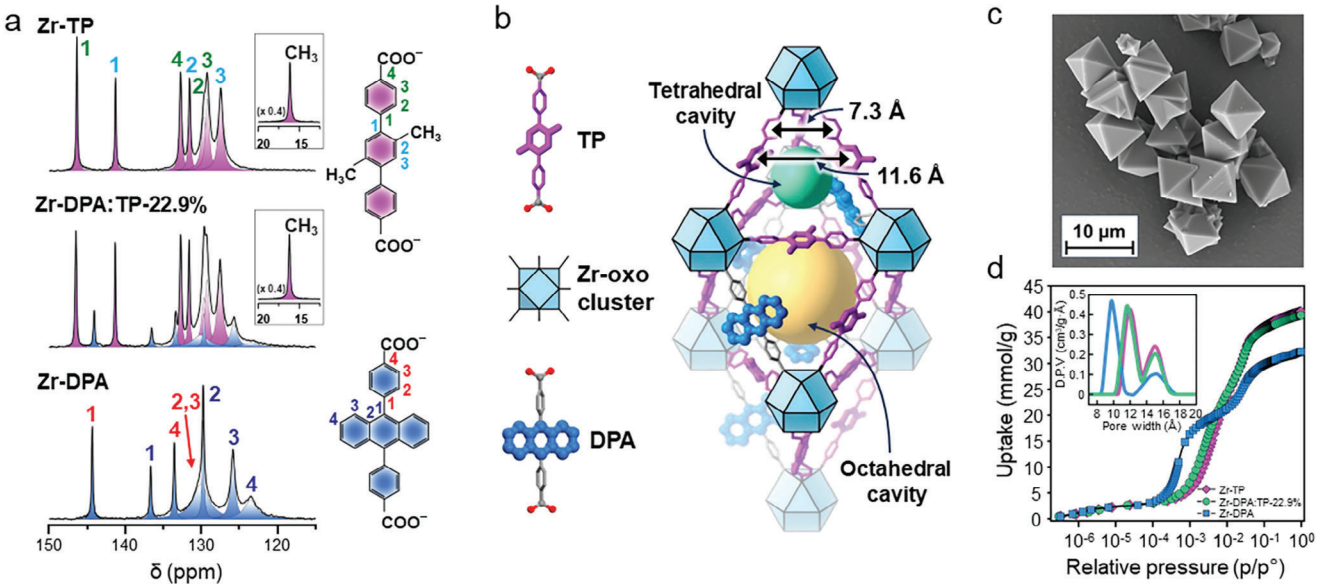

Figure 3. a) ^{13}C {^{1}H} CP MAS NMR spectra of Zr-TP, Zr-DPA:TP-22.9% and Zr-DPA performed at room temperature, 7.04 T, with a spinning speed of 12.5 kHz and a contact time of 2 ms. b) Molecular structure of TP and DPA ligands and metal node. Crystal structure of Zr-DPA:TP displaying the tetrahedral and octahedral cavities (yellow and green spheres). c) SEM images of sample Zr-DPA:TP-22.9% (scale bar = 10 μm). d) N_2 adsorption isotherms of Zr-TP (pink diamonds), Zr-DPA:TP-22.9% (green circles), and Zr-DPA (blue square) collected at 77 K displayed in semilogarithmic plot. Inset: pore size distribution in the micropore region.

parameters. Scanning electron microscopy (SEM) images unveiled the octahedral morphology of the MOF crystals (Figure 3c; Figures S16–S24, Supporting Information). The permanent porosity of the Zr-MOFs was demonstrated by N_2 adsorption isotherms collected at 77 K (Figure 3d). Surface areas higher than 3900 m^2/g and ≈ 3600 m^2/g were calculated according to Langmuir and BET models, respectively (Figure S40–S46 and S57; Tables S9 and S14, Supporting Information). The pore volume of the hetero-ligand Zr-MOFs linearly decreased on increasing DPA content since the anthracene moiety of DPA occupies a much larger volume than the dimethylphenyl group of TP. A two-step profile at low partial pressure is observed owing to the filling of the tetrahedral and octahedral cavities as observed by the pore size distribution: the diameters of the tetrahedral pores diminished on increasing the DPA content (from 10.9 to 10.4 Å) whilst the size of the octahedral cavities is of 14.8 Å, as determined by NL-DFT theory (HS-2D-NLDFT carbon model). ^{1}H MAS and ^{13}C CP MAS solid-state NMR spectra demonstrate the purity of the samples and the presence of both DPA and TP ligands in the frameworks (Figure 3a). The extremely sharp resonances of the spectra are diagnostic of the high crystallinity of the compounds and enable the assignment of all the peaks. The ^{13}C CP MAS NMR spectrum of Zr-DPA:TP-22.9%, shown in Figure 3a, highlights in the aromatic region the signals characteristic of DPA moiety and those attributed to the TP group (blue and pink signals, respectively). Additionally, a marked resonance in the aliphatic region (δ_C = 16.2 ppm, Table S10, Supporting Information) confirms the presence of methyl groups bonded to the central TP ring. The amount of the OH groups coordinated to the Zr ions in the cluster was estimated by ^{1}H MAS NMR (δ_{OH} = 2.5 ppm and 3.1 ppm for Zr-TP and Zr-DPA, respectively, Table S11, Supporting Information), which agrees with the charge-balanced stoichiometry of the crystal structures (Figures S52 and S54, Supporting Information).

3. Energy Transfer Processes in Hetero-Ligand MOFs and their Scintillation Properties

To further investigate the effectiveness of the energy transfer process between TP and DPA, the Förster interaction radius R_{Fs}, that is the distance at which the energy transfer efficiency is 50%,[15] has been evaluated in cyclohexane solution for the TP/DPA donor/acceptor pair. **Figure** 4a shows the results obtained for the measurement of the energy transfer yield ϕ_{ET} as a function of the DPA concentration (Section S1, Supporting Information). Given the small ligand molecular size and the low solvent viscosity, the energy transfer process was modeled considering the rapid diffusion limit.[16] The energy transfer rate k_{ET} can be then calculated as

$$k_{ET} = \frac{4\pi k_D C R_{Fs}^6}{3a^3}, \quad (1)$$

where $k_D = k_{TP}$ is the donor/TP emission decay rate, C is the acceptor concentration, and a = 1.2 nm is the minimum contact distance between donor and acceptor approximated as spheres with radii of 7.5 and 4.5 Å for TP and DPA, respectively. Considering that ϕ_{ET} is defined as

$$\phi_{ET} = \frac{k_{ET}}{k_{ET} + k_{TP}}, \quad (2)$$

Equations (1) and (2) can be used to fit the experimental data. The solid line in Figure 4a shows the best fit for the TP→DPA

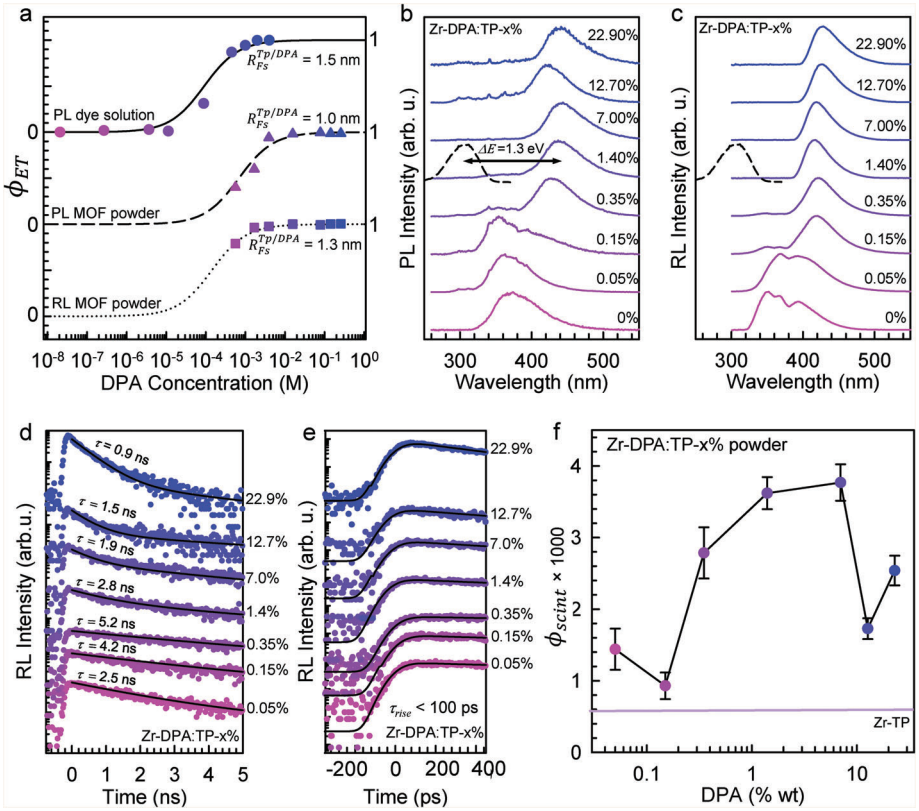

Figure 4. a) Resonance energy transfer efficiency measured for the TP/DPA donor/acceptor pair in cyclohexane solution and for Zr-DPA:TP-x% MOFs series. Lines are the fit of data with a model of the Förster energy transfer process in the rapid diffusion limit with characteristic interaction radius $R_{Fs}^{Tp/DPA}$. b) Photoluminescence (PL) spectra of the Zr-DPA:TP-x% under UV laser excitation at 250 nm. The black dashed line is the TP ligand optical absorption spectrum. c) Radioluminescence (RL) spectra of the Zr-DPA:TP-x% series under soft X-ray irradiation. d) Scintillation pulses of the Zr-DPA:TP-x% series recorded at 440 nm under pulsed soft X-ray excitation and e) focus on the scintillation pulses rise time. Solid lines are the fit of the data considering the scintillation pulse convoluted to the instrumental time response (X-rays pulse FWHM = 140 ps). f) Scintillation light yield (ϕ_{scint}) of the Zr-DPA:TP-x% series under soft X-ray excitation.

energy transfer yield in cyclohexane solution measured as a function of the DPA concentration, which results in a radius $R_{Fs}^{Tp/DPA}$ = 1.5 nm for the TP/DPA pair in cyclohexane.

The emission properties of the MOF series have been investigated using continuous wave (*cw*) and time-resolved photoluminescence and scintillation experiments. Figure 4b,c shows, respectively, the *cw* photoluminescence and radioluminescence spectra of the Zr-DPA:TP-x% MOFs series. Considering the crystal structure and the TP singlet exciton diffusivity, the rapid diffusion regime in the MOF environment can still be valid, even if the diffusion coefficients are underestimated while neglecting exchange interactions (Section S1.3, Supporting Information). Indeed, by combining Equations (1) and (2), the experimental ϕ_{ET} values derived by analyzing the TP emission intensity as a function of DPA concentration are well reproduced. The fit procedure results in an interaction radius of 1.0 and 1.3 nm from the photoluminescence and radioluminescence data, respectively, in good agreement with the results obtained in the solution. Interestingly, a complete energy transfer with $\phi_{ET}^{1.4\%} = 0.98$ is obtained already with a very low 1.4%wt loading of DPA. This is about one order of magnitude lower than the previous case study,[7] thus completely abating re-absorption effects by achieving a huge Stokes shift as large as 1.35 eV (Figure 4b). Moreover, by Equation (2) we can directly evaluate the transfer rate for this specific sample, which results as high as $k_{ET}^{1.4\%} \approx 50$ GHz. This demonstrates that in this system the energy transfer from excited TPs to DPA molecules occurs in ≈20 ps, an almost ultrafast time scale as expected considering the electronic properties of the TP ligand discussed above despite being a diffusion-mediated process.[11,17] By increasing the DPA concentration the transfer is faster, thus reaching the picosecond time range for the more loaded crystals (Table S2, Supporting Information).

The high efficiency of the energy transfer mechanism is confirmed by the analysis of the TP photoluminescence lifetime in the sample series (Figure S4, Supporting Information). In all the MOFs only a very weak, slow signal from TP can be recorded with a few nanosecond lifetime, which is consistent with the existence of statistically partially doped systems.[7] This finding further demonstrates that at any of the DPA concentrations employed the energy transfer is effective, in agreement with the k_{ET} values calculated by Equation (1) from the experimental data (Table S1, Supporting Information). Even the lowest DPA loading of 0.05%wt shows a $\phi_{ET} \approx 0.80$ indicating a $k_{ET}^{0.05\%}$ as large as at least 4 GHz, which is much higher than the spontaneous TP decay rate $k_{TP} = (\tau_{TP})^{-1} = 1$ GHz and therefore undetectable with the available experimental setup (Experimental Section).

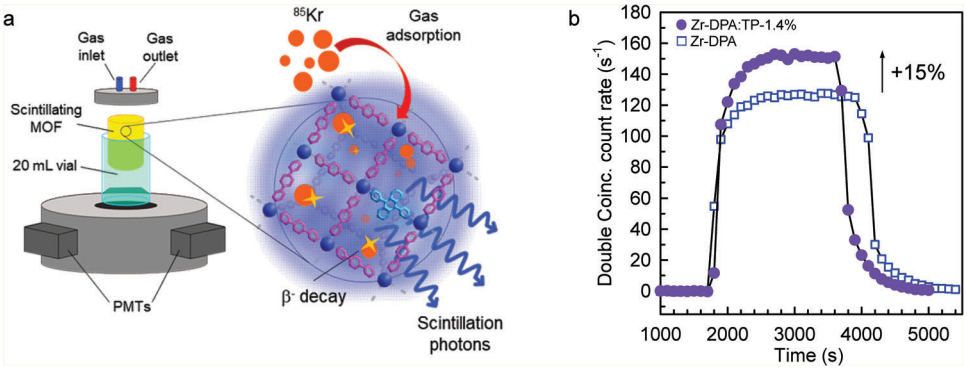

Figure 5. a) Sketch of the time coincidence-based system employed for radioactive gas detection. A mix of air and ^{85}Kr diffuses into a glass chamber containing the porous scintillating MOFs. The gas, adsorbed in the material, undergoes radioactive decay by emitting β^- particles that ionize the MOF. The free charges generated by this event readily recombine on the active TP sites, transferring their energy to neighboring DPA molecules, producing the scintillation emission. The emitted photons are collected by two photomultiplier (PMT) tubes working in coincidence. b) ^{85}Kr detection for Zr-DPA (squares) and Zr-DPA:TP-1.4% MOFs (circles).

Ultrafast scintillation experiments confirm this picture. Figure 4d shows the scintillation pulses of the Zr-DPA:TP-x% MOF series under pulsed X-rays recorded at 440 nm. All samples show multi-exponential emission decay kinetics with different average lifetimes, thus suggesting a composition-dependent effect on the presence of a distribution of defects/electronic traps in the framework that partially quench the DPA luminescence.[18] On the other hand, all the compounds show an ultrafast rise time of the emission undistinguishable from the excitation X-ray pulse (Experimental Section) and in agreement with the expected k_{ET} values. The beneficial effect of the DPA co-ligand's presence on the MOF emission properties is evident by analyzing the data reported in Figure 4f. The plot reports the scintillation efficiency, that is the light yield ϕ_{scint} defined as the ratio between the number of emitted photons for each MeV of energy deposited by the ionizing radiation, measured as a function of the DPA loading (Experimental Section). The ϕ_{scint} is the highest for Zr-DPA:TP-1.4% and Zr-DPA:TP-7.0%, reaching ≈ 3800 ph MeV^{-1}, which is about five times that of the parent Zr-TP MOF (ϕ_{scint} = 800±105 ph MeV^{-1}). Interestingly, the Zr-DPA:TP-1.4% specimen exhibits the highest ϕ_{scint} despite the partially quenched emission and the low amount of acceptor employed, thus suggesting the crucial role of the re-absorption elimination in the observed light output enhancement.

4. Detection of Radioactive Gas by Hetero-Ligand MOFs

Owing to its high surface area and pore capacity, the highly emissive and reabsorption-free Zr-DPA:TP-1.4% MOF was tested for the detection of the noble gas radioactive isotope 85-krypton (^{85}Kr). Notably, Kr adsorption isotherms collected from 273 to 298 K and up to 1 bar pointed out that Kr can be adsorbed inside the cavities even under mild conditions of pressure and temperature (Figures S58 and S60; Tables S15 and S16, Supporting Information), comparable with the working conditions for radioactive-gas detection. The strength of the interactions between the Kr atoms and the pore surface was determined according to the Van't Hoff equation. The isosteric heat of adsorption for Kr (Q_{st}) at low loadings was evaluated to be 16.0 ± 0.5 kJ mol^{-1} (Figures S59, S61 and S62, Supporting Information), a value comparable to that of UiO-66, the progenitor of the Zr-MOF family.[19] The Zr-DPA:TP-1.4% has been tested for ^{85}Kr detection employing a time coincidence measurement technique using two photomultiplier tubes (PMTs) simultaneously (Methods).[6a,b,20] The decay of ^{85}Kr nuclei produces β^- particles with 687.1 keV maximum energy and an average energy of 251.4 keV.[21] As shown in **Figure 5a**, in our setup, MOF powder (100 mg) is poured into a cylindrical glass chamber of 0.5 cm thickness, and a mix of air and ^{85}Kr is allowed to flow through it. The ^{85}Kr atoms are, therefore, adsorbed and concentrated in the pores. In such a way, the total activity is measured by recording the scintillation photons produced by MOFs upon interaction with β^- particles using two PMTs that work in coincidence, allowing for better event discrimination and increasing the signal-to-noise ratio.[22] The Zr-DPA:TP-1.4% sample has been tested in comparison with the previously tested reference compound, the *homo*-ligand Zr-DPA system.[9] Figure 5b shows the results of the ^{85}Kr detection experiment for both samples by applying the technique with a coincidence window of 40 ns. Under the same experimental conditions, the hetero-ligand MOF shows a net +15% in the ^{85}Kr detection capability due to its improved scintillation efficiency and re-absorption elimination, thus strongly encouraging the use and further development of large Stokes shift MOFs for photonic application in bulk devices. We note that the observed enhancement is less than the expected. We ascribe this fact to the trapping of scintillation photons within the highly-scattering and bulky MOF powder sample required to harvest and concentrate the gas radionuclides. The photons generated in the inner part of the powder travel for a significantly longer path with respect to the ones generated on the sample surface before exiting to be recorded by the PMTs, thus enhancing the probability to be re-absorbed by the DPA ligands in the MOF despite their extremely low amount and weak absorption coefficient (Figure S4, Supporting Information). This partially limits the detection sensitivity enhancement.

5. Conclusion

To summarize, we successfully designed, engineered, and synthesized hetero-ligand scintillating MOF crystals, obtaining a

Stokes shift larger than 1.3 eV, from the UV to the visible spectral region by embedding two types of conjugated ligands with complementary optical absorption and emission properties. The specific electronic properties of the TP ligands enable the optimization of the energy transport within the MOF platform, and the energy transfer to the energy acceptor ligands, thus instantaneously activating the crystal's highly Stokes-shifted fluorescence through an ultrafast energy transfer process that can occur in the picoseconds time scale. Owing to these extremely efficient energy transport mechanisms, we can minimize the loading level of the energy acceptor moiety, thus completely avoiding the reabsorption of its emission and achieving a significant increment of the crystal scintillation efficiency.

In the optimized composition, the hetero-ligand MOF showed a net improvement in its ability to detect the ^{85}Kr gas radionuclide with respect to the reference homo-ligand counterpart, thus demonstrating the effectiveness of the proposed strategy for fabrication of efficient large Stokes shift fast emitters for technological applications in bulk devices. The obtained result demonstrates that the MOF energy transport properties can be further developed and refined by controlling the fundamental electronic properties of their ligand building blocks including also their molecular orbital wavefunction shape and spatial delocalization to actively control short-range exchange interactions within adjacent framed conjugated species, possibly involving coherent processes,[17] or hot excited states coupling.[23] These engineered hetero-ligand MOFs will show improved emission efficiency and ultrafine control of energy transport and transfer promising new breakthroughs in consolidated applications, such as highly efficient spatially controlled selective photoreactions,[24] or full access to embryonal research fields, such as for the realization of new materials for quantum sensing and information.[25,26]

6. Experimental Section

Synchrotron Radiation PXRD Experimental Conditions: Samples were prepared and sealed in 0.5 mm Lindeman capillaries for XRD experiments at the ESRF ID22 beamline using a 0.354 Å wavelength. PXRD measurements were collected over a 2θ angle range of 0.0 – 32.0° with a data collection interval of 0.002° and data collection was done over 12 detectors simultaneously. The scan speed varied depending on sample degradation. Data were collected on various spots along the capillary and multiple times on the same spot. Any scans that showed signs of degradation were excluded from the final merged and binned data set.

High-Resolution SEM: Scanning electron microscopy (SEM) images were collected using a Zeiss Gemini 500 microscope, operating at 5 KV. The microcrystalline powders were deposited on a conductive tape, dried under a high vacuum, and sputtered with gold before the analysis (10 nm, nominal thickness).

Gas Adsorption: Adsorption experiments were performed using gases with the purity of 5.0 (N_2, He, Kr). N_2 adsorption isotherms at 77 K and Kr adsorption isotherms at 273, 283, 293, and 298 K were collected on a Micromeritics 3Flex Adsorption Analyzer. The samples were treated at 100 °C under vacuum before sorption measurements. Bath temperature was controlled using a Julabo F32-HE HighTech Refrigerated/Heating Circulator.

Photoluminescence Studies: All experiments have been performed on activated MOF crystalline powders. TP and DPA absorption spectra were recorded with a Cary Lambda 900 spectrophotometer at normal incidence using quartz Suprasil cuvettes with 0.1 cm of optical path. Steady-state photoluminescence (PL) and excitation PL (PLE) spectra were acquired with a Variant Eclipse fluorimeter (bandwidth 1 nm) using quartz Suprasil cuvettes with 1 cm of optical path. The TP PL quantum yield was measured with relative methods using PPO as UV fluorescence standard.[27] Time-resolved photoluminescence experiments in the nanosecond time scale were carried out by using as an excitation source a pulsed laser LED at 340 nm (3.65 eV, EP-LED 340 Edinburgh Instruments) or 250 nm (4.96 eV, EP-LED 250 Edinburgh Instruments), coupled to FLS980 Edinburgh setup in Time-Correlated Single Photon Counting (TCSPC) acquisition mode. The overall time resolution of the setup was 300 ps.

Scintillation Studies: Steady-state radioluminescence (RL) measurements were carried out at room temperature using a homemade apparatus featuring, as a detection system, a liquid nitrogen-cooled, back-illuminated, and UV-enhanced charge-coupled device (CCD) Jobin-Yvon Symphony II, combined with a monochromator Jobin-Yvon Triax 180 equipped with a 100 lines mm^{-1} grating. All spectra are corrected for the spectral response of the detection system. RL excitation was obtained by unfiltered X-ray irradiation through a Be window, using a Philips 2274 X-ray tube with a tungsten target operated at 20 kV. At this operating voltage, a continuous X-ray spectrum is produced by a Bremsstrahlung mechanism superimposed to the L and M transition lines of tungsten, due to the impact of electrons generated through the thermionic effect and accelerated onto a tungsten target. Time-resolved scintillation spectra were collected by means of an FLS980 spectrometer (Edinburgh Instruments) coupled to a PicoHarp 300 multichannel scaler and a PMA Hybrid photomultiplier (Picoquant PMA-06) as photodetector working in time-correlated single photon counting (TCSPC) mode (time resolution ≈4 ps). X-ray pulses are generated using a 405 nm ps-pulsed laser (Edinburgh Instruments, EPL-405) to activate the photocathode of the N5084 Hamamatsu X-ray tube with an applied voltage of 40 kV. The average energy of the generated X-rays is 14.5 keV with a pulse width of 160 ps. The MOF scintillation yield ϕ_{scint} has been measured by relative methods using the BGO crystal powder as reference (ϕ_{scint} = 10^4 ph MeV^{-1}). The typical relative uncertainty of this measurement was 20%.

Radioactive Gas Detection Experiments: The experiments were performed using a gas bench developed at the CEA, Paris-Saclay,[28] and by allowing the production of radioactive gas atmospheres using high activity standards. Different sampling and dilution steps allow for precise control of the injected activity, and precise knowledge of the volumetric activity of each gas: at best, the relative standard uncertainty on the activity concentration was 0.4%, 0.6%, and 0.8% for ^{222}Rn, ^{85}Kr and ^{3}H, respectively (Table S9, Supporting Information). A reference instrument developed at CEA the micro-TDCR, that is, a metrological device developed to exploit the triple-to-double coincidence ratio,[20] was connected to the test bench allowing closed-loop circulation of the radioactive gas inside the vial containing the scintillator material, here the MOF. For each experiment, the same type of three-step sequence was performed. First, the measurement of the blank, by circulating clean air without additional radioactivity. Second, the measurement of scintillation by circulating the radioactive gas sample into the vial (here a glass tube of 4 mm diameter and 50 mm height containing the MOF powder). Third, the circulation of clean air into the device to remove the radioactive gas. The light photons produced by scintillation are measured by the micro-TDCR with a specific connection cap adapted to the radioactive gas flow in the scintillator. The counting units allow to use of three photomultiplier tubes (PMTs) to count double coincidences (D) and triple coincidences (T) between the PMTs. The ratio T/D was a great indicator of the scintillation efficiency while the D count rate was used to calculate the activity and thus to obtain the overall efficiency of the counting unit, that was the scintillators and the whole device.

Supporting Information

Supporting Information is available from the Wiley Online Library or from the author.

Acknowledgements

M.O. and J.P. contributed equally to this work. The authors acknowledge support from the European Community through the grant no. 899293,

HORIZON 2020 – SPARTE FET OPEN. Financial support from the Italian Ministry of University (MUR) through grant PRIN 2020 – SHERPA no. H45F2100343000, PRIN-2022 – HYSTAR no. H53D23004720006 and grant MINERVA LuMIminesceNt scintillating hEterostructures foR adVanced medical imaging no. H25E22000490006. The Lombardy Region for "Enhancing Photosynthesis" grant (2021-2023) was acknowledged for the financial support. The authors are grateful to the ESRF synchrotron facility in Grenoble (France) for access to the ID22 beamline (Project: HC-5193).

Conflict of Interest

The authors declare no conflict of interest.

Data Availability Statement

The data that support the findings of this study are available from the corresponding author upon reasonable request.

Keywords

energy transfer, metal–organic frameworks, porous materials, radionuclides, scintillation, Stokes shift

Received: March 14, 2024
Revised: May 14, 2024
Published online: May 27, 2024

[1] J. Zhang, R. Chen, Z. Zhu, C. Adachi, X. Zhang, C.-S. Lee, *ACS Appl. Mater. Interfaces* **2015**, *7*, 26266.
[2] S. Mattiello, A. Sanzone, F. Bruni, M. Gandini, V. Pinchetti, A. Monguzzi, I. Facchinetti, R. Ruffo, F. Meinardi, G. Mattioli, M. Sassi, S. Brovelli, L. Beverina, *Joule* **2020**, *4*, 1988.
[3] a) T.-B. Ren, W. Xu, W. Zhang, X.-X. Zhang, Z.-Y. Wang, Z. Xiang, L. Yuan, X.-B. Zhang, *J. Am. Chem. Soc.* **2018**, *140*, 7716; b) X. Wang, H. Shi, H. Ma, W. Ye, L. Song, J. Zan, X. Yao, X. Ou, G. Yang, Z. Zhao, *Nat. Photonics* **2021**, *15*, 187.
[4] a) A. Ronchi, C. Capitani, V. Pinchetti, G. Gariano, M. L. Zaffalon, F. Meinardi, S. Brovelli, A. Monguzzi, *Adv. Mater.* **2020**, *32*, 2002953; b) P. Mondal, S. Chakraborty, G. K. Grandhi, R. Viswanatha, *J. Phys. chem. Lett.* **2020**, *11*, 5367.
[5] P. Lecoq, M. Korzhik, A. Vasiliev, *IEEE Trans. Nucl. Sci.* **2013**, *61*, 229.
[6] a) M. Orfano, J. Perego, F. Cova, C. X. Bezuidenhout, S. Piva, C. Dujardin, B. Sabot, S. Pierre, P. Mai, C. Daniel, *Nat. Photonics* **2023**, *17*, 672; b) S. Mauree, V. Villemot, M. Hamel, B. Sabot, S. Pierre, C. Dujardin, F. Belloni, A. Comotti, S. Bracco, J. Perego, *Adv. Funct. Mater.* **2023**, *33*, 2302877.
[7] J. Perego, C. X. Bezuidenhout, I. Villa, F. Cova, R. Crapanzano, I. Frank, F. Pagano, N. Kratochwill, E. Auffray, S. Bracco, *Nat. Commun.* **2022**, *13*, 3504.
[8] Q. Liu, Q. Wang, M. Xu, J. Liu, J. Liang, *Spectrochim. Acta, Part A* **2020**, *227*, 117627.
[9] C. Mahmoudi, R. Chouk, K. Baatout, N. S. Jaballah, M. Khalfaoui, M. Majdoub, *J. Mol. Struct.* **2022**, *1251*, 131993.
[10] a) C. Zener, R. R. Heikes, *Rev. Mod. Phys.* **1953**, *25*, 191; b) M. Inokuti, F. Hirayama, *J. Chem. Phys.* **1965**, *43*, 1978; c) J. Cornil, D. Beljonne, J.-P. Calbert, J.-L. Brédas, *Adv. Mater.* **2001**, *13*, 1053.
[11] G. D. Scholes, *Annu. Rev. Phys. Chem.* **2003**, *54*, 57.
[12] J. H. Cavka, S. Jakobsen, U. Olsbye, N. Guillou, C. Lamberti, S. Bordiga, K. P. Lillerud, *J. Am. Chem. Soc.* **2008**, *130*, 13850.
[13] a) A. Schaate, P. Roy, A. Godt, J. Lippke, F. Waltz, M. Wiebcke, P. Behrens, *Chem.–A European J.* **2011**, *17*, 6643; b) Y. Bai, Y. Dou, L.-H. Xie, W. Rutledge, J.-R. Li, H.-C. Zhou, *Chem. Soc. Rev.* **2016**, *45*, 2327.
[14] L. Valenzano, B. Civalleri, S. Chavan, S. Bordiga, M. H. Nilsen, S. Jakobsen, K. P. Lillerud, C. Lamberti, *Chem. Mater.* **2011**, *23*, 1700.
[15] J. B. Birks, *Photophysics of aromatic molecules*, Wiley-Interscience, London **1970**.
[16] D. D. Thomas, W. F. Carlsen, L. Stryer, *Proc. Natl. Acad. Sci. USA* **1978**, *75*, 5746.
[17] C. A. Rozzi, S. M. Falke, N. Spallanzani, A. Rubio, E. Molinari, D. Brida, M. Maiuri, G. Cerullo, H. Schramm, J. Christoffers, C. Lienau, *Nat. Commun.* **2013**, *4*, 1602.
[18] a) X.-S. Wang, T. E. Dykstra, M. R. Salvador, I. Manners, G. D. Scholes, M. A. Winnik, *J. Am. Chem. Soc.* **2004**, *126*, 7784; b) J. Gierschner, L. Lüer, B. Milián-Medina, D. Oelkrug, H.-J. Egelhaaf, *J. Phys. Chem. Lett.* **2013**, *4*, 2686.
[19] Y. Yang, C. Tu, L. Guo, L. Wang, F. Cheng, F. Luo, *Cell Reports Phys. Sci.* **2023**, *4*, 101694.
[20] B. Sabot, C. Dutsov, P. Cassette, K. Mitev, *Nucl. Instrum. Methods Phys. Res., Sect. A* **2022**, *1034*, 166721.
[21] M.-M. Bé, V. Chisté, C. Dulieu, E. Browne, C. Baglin, V. Chechev, N. Kuzmenko, R. L. Helmer, F. Kondev, T. D. Macmahon, K. B. Lee, Table of Radionuclides, Bureau International des Poids et Mesures, BIPM, Pavillon de Breteuil, Sevres Cedex, France **2006**.
[22] C. Dutsov, P. Cassette, K. Mitev, B. Sabot, *Nucl. Instrum. Methods Phys. Res., Sect. A* **2021**, *987*, 164846.
[23] A. J. Sneyd, T. Fukui, D. Paleček, S. Prodhan, I. Wagner, Y. Zhang, J. Sung, S. M. Collins, T. J. A. Slater, Z. Andaji-Garmaroudi, L. R. MacFarlane, J. D. Garcia-Hernandez, L. Wang, G. R. Whittell, J. M. Hodgkiss, K. Chen, D. Beljonne, I. Manners, R. H. Friend, A. Rao, *Sci. Adv.* **2021**, *7*, eabh4232.
[24] Q. Wang, Q. Gao, A. M. Al-Enizi, A. Nafady, S. Ma, *Inorg. Chem. Front.* **2020**, *7*, 300.
[25] A. Kultaeva, A. Pöppl, T. Biktagirov, *J. Phys. Chem. Lett.* **2022**, *13*, 6737.
[26] L. Sun, L. Yang, J.-H. Dou, J. Li, G. Skorupskii, M. Mardini, K. O. Tan, T. Chen, C. Sun, J. J. Oppenheim, R. G. Griffin, M. Dincă, T. Rajh, *J. Am. Chem. Soc.* **2022**, *144*, 19008.
[27] I. Berlman, *Handbook of florescence spectra of aromatic molecules*, Elsevier, Amsterdam New York, **2012**.
[28] B. Sabot, M. Rodrigues, S. Pierre, *Appl. Radiat. Isot.* **2020**, *155*, 108934.